Highly Efficient Photon Energy Conversion and Ultrasensitive Self-Powered Photodetection via a Monolithic p-3C-SiC Nanothin Film on p-Si/n-Si Double Junction

Dinh Gia Ninh,* Minh Tam Hoang, Tuan-Hung Nguyen, Erik Streed, Sima Dimitrijev, Philip Tanner, Tuan-Khoa Nguyen, Nam-Trung Nguyen, Hongxia Wang, Yong Zhu, Van Dau, and Dzung Viet Dao

ACCESS | ᐧᐧᐧ Metrics & More | ᐧᐧᐧ Article Recommendations | ᐧᐧᐧ Supporting Information

ABSTRACT: The pursuit of increased efficiency of photoelectric energy conversion through optimized semiconductor structures remains highly competitive, with current results yet to align with broad expectations. In this study, we discover a significant enhancement in photocurrent performance of a p-3C-SiC nanothin film on p-Si/n-Si double junction (DJ) heterostructure that integrates p-3C-SiC/p-Si heterojunction and p-Si/n-Si homojunction. The vertical photocurrent (VPC) and vertical photoresponsivity exhibit a substantial enhancement in the DJ heterostructure, surpassing by a maximum of 43-fold compared to the p-3C-SiC/n-Si single junction (SJ) counterpart. The p-3C-SiC layer and n-Si substrate of the two heterostructures have similar material and geometrical properties. More importantly, the fabrication costs for the DJ and SJ heterostructure devices are comparable. Our results demonstrate a significant potential for using DJ devices in energy harvesters, micro/nano electromechanical systems, and sensing applications. This research may also lead to the creation of advanced optoelectronic devices using DJ structures, where employing various semiconductor materials to achieve exceptional performance through the application of the concept and theoretical model described in this work.

n-Si (500 μm) ⬜ p-Si (1 μm) ⬜ p-3C-SiC (500 nm)
Electrodes ● Holes ● Electrons

KEYWORDS: silicon carbide, double junction, single junction, optoelectronic characteristics, photodetectors
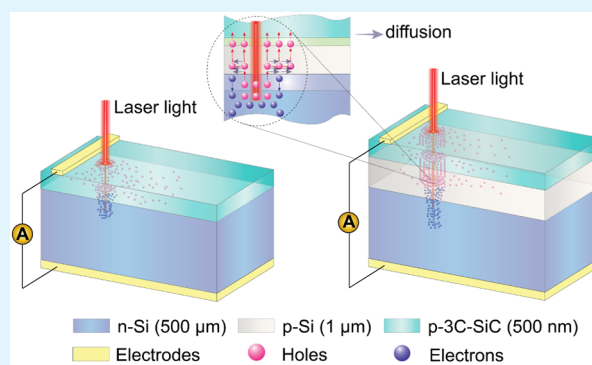
1. INTRODUCTION

As the world faces problems of energy depletion and increasing environmental pollution, green and renewable energy sources have become increasingly important and have attracted many experts to this emerging field. Self-powered devices, particularly those that rely on natural light energy, are being extensively investigated and developed for energy harvesting, microelectromechanical systems (MEMS), nanoelectromechanical systems (NEMS), and solar cells. In self-powered modes, multijunction (MJ) structures outperform single junction (SJ) structures[1,2−5] due to the creation of multiple electron-hole pairs, longer carrier lifetimes, and wider bandgaps. However, because of the substantially higher production cost compared to SJ counterparts, the prices of devices incorporating MJ structures are also significantly higher than those using SJ structures.[1,6,7] Furthermore, the world economy is suffering several challenges as a consequence of the ongoing COVID-19 pandemic. Thus, high-performance and low-cost products are the top priority of industries. In this study, we explored a double junction (DJ) structure with three layers of monolithically integrated semiconductor materials that cost the same as an SJ structure. In addition, experimental

data obtained for the photodetection properties of this bijunction device indicate its superiority over those in the SJ device. This achievement marks a significant breakthrough in advancing MEMS, NEMS, and energy-harvesting applications.

In terms of optoelectronic devices, photodetectors are dominant structures because of their superiority in generating large photocurrents and high sensitivity with massive potential for use in energy harvesting applications. High-performance photodetectors based on 2D materials,[8−11] graphene,[12−15] and perovskite[16−19] have been intensively developed in recent years. However, silicon still dominates solid-state electronics for half a century due to its excellent properties and the maturity of the semiconductor industry. The related manufacturing processes of silicon are simpler than those of other materials. Many types of semiconductors can be
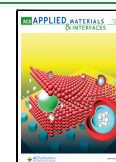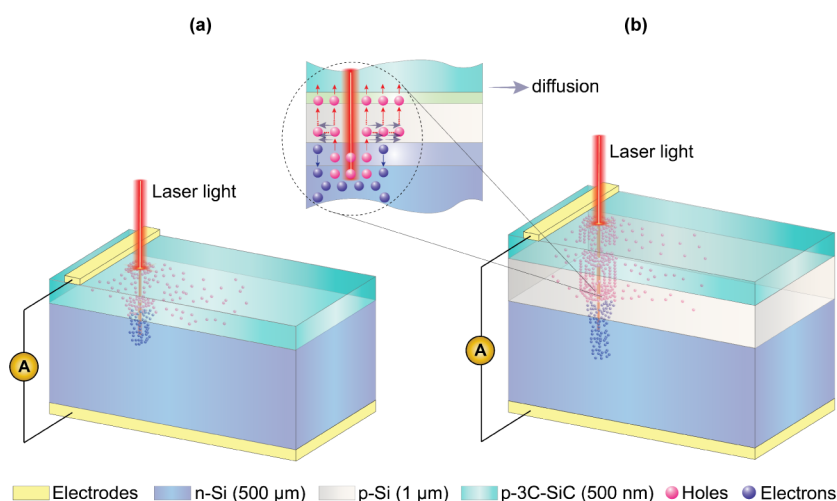
Figure 1. Designed SJ and DJ devices under laser light. (a) p-3C-SiC/n-Si; (b) p-3C-SiC/p-Si/n-Si.

combined with silicon to form unique structures for use in MEMS and NEMS devices, such as ZnO-WS2/Si,[20] ZnGa2O4/Si,[21] graphene-Si,[22] reduced graphene oxide (rGO)/n-Si,[23] n-Si(111)/TiO$_2$ nanorod,[24] MoS$_2$/Si nanowire,[25] MoS$_2$/Si homotype heterojunction,[26] and InGaAs/Si.[27] Silicon carbide (SiC) is a material that can be delicately integrated with Si and can operate under extreme conditions.[28−30] Cubic silicon carbide (3C-SiC) is a polytype of the silicon carbide family that is commercially employed with two other polytypes, 4H and 6H. However, 3C-SiC on Si has a lower manufacturing cost than other polytypes[31] such as 4H-SiC and 6H-SiC; thus, it is more commonly utilized in electronic devices. The monolithic integration of a 3C-SiC thin film on double Si, resulting in a structure of p-3C-SiC on a p-Si/n-Si double junction, is the novelty of the current study. Here, p-3C-SiC on p-Si is a heterojunction, whereas p-Si on n-Si is a homojunction. The vertical optoelectronic characteristics of the DJ heterostructures were compared with those of the SJ structure (p-3C-SiC on Si). Notably, the p-3C-SiC thin film and n-Si of both structures are the same in all parameters. The obtained results demonstrate the superiority of the DJ device over the SJ device, opening a new avenue for the development of high-performance yet low-cost MEMS and NEMS self-powered devices and energy harvesters. The design principle employed in creating the p-3C-SiC/p-Si/n-Si DJ device shown in this study can also be extended to other semiconductor materials, thereby enabling performance enhancement compared to their SJ counterparts. Therefore, four major advances have been achieved in this study:

(i). Superior optoelectronic characteristics of the DJ structure are shown as compared to SJ counterpart. The DJ structure exhibits a vertical photoresponsivity, and vertical photocurrent of over 40 times greater than those of the 3C-SiC/Si single junction (SJ) counterpart, which shares similarities in all technical parameters, except for the inclusion of a middle Si layer in the DJ structure. The main disparity resides in the presence of the p-Si layer situated within the core of the DJ structure.

(ii). The notable contribution of this study lies in the method employed to produce these structures, which is exceptionally straightforward yet ensures high precision. Utilizing low-pressure chemical vapor deposition (LPCVD) at around 1,100 °C is a remarkably simple process

within cleanroom environments, allowing for the simultaneous production of large batches of wafers. This approach offers significantly greater cost-effectiveness and time efficiency when compared to the fabrication of other semiconductor structures, such as perovskite cells. Furthermore, the materials used in this study, silicon carbide (SiC) nanothin film, exhibit excellent performance in harsh environments and at very high temperatures, a characteristic that perovskite cannot reliably provide.

(iii). Equivalent costs are realized for the production and manufacturing of DJ and SJ devices. This demonstrates our ability to address both the technical and economic challenges. In previous research, it has been demonstrated that the production of double junction or multijunction structures is considerably more expensive when compared to single-junction structures. Therefore, the nearly equivalent manufacturing costs of these two types of structures discussed in this article constitute a substantial advantage.

(iv). This design and physic principles are potentially useful for other semiconductor materials to enhance photodetector characteristics for diverse structures. Adding just one p-Si layer in the middle results in a notable enhancement, explained by the efficient photogeneration of charge carriers, electron-hole pair separation, modulation of energy bands, and the mechanisms of the charge carrier transport. These interesting physical phenomena and mechanisms hold potential for application across various semiconductor architectures.

2. DESIGN OF THE P-3C-SIC/P-SI/N-SI DJ HETEROSTRUCTURE

2.1. Two Designed Heterostructures. To achieve superior vertical optoelectronic characteristics in self-powered mode, i.e., no electrical power is supplied to the device, a p-3C-SiC/p-Si/n-Si double junction (DJ) device was designed, fabricated, evaluated, and compared with a p-3C-SiC/n-Si single junction (SJ) device under identical working conditions. Figure 1 shows the designed SJ and DJ devices under laser light. The only difference between the DJ and SJ heterostructure devices is the p-Si middle layer in the DJ heterostructure. This p-Si middle layer is expected to enhance charge carrier generation and transportation, resulting in a larger photocurrent, as depicted in Figure 1b. In the
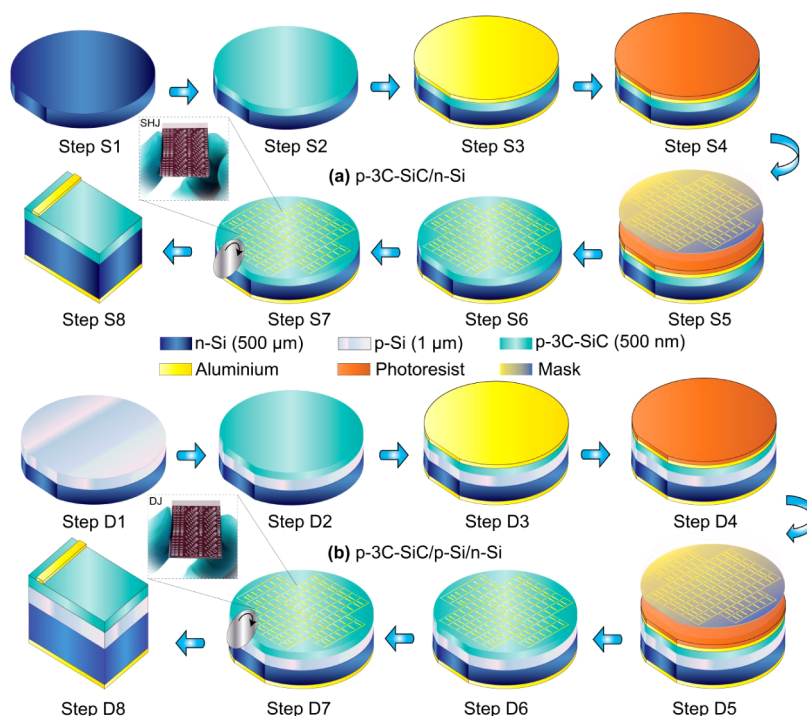
Figure 2. Fabrication process and design of the (a) p-3C-SiC/n-Si device and (b) p-3C-SiC/p-Si/n-Si device. Note that Steps S1–S2 and Steps D1–D2 were implemented by D&X Co., Ltd. (Supporting Information). Step S1: preparation of n-Si wafer; Step S2 and Step D1: growth of p-3C-SiC on n-Si substrate and growth of p-Si on n-Si substrate by low pressure chemical vapor deposition (LPCVD) technique, respectively; Step D2: growth of p-3C-SiC on p-Si/n-Si by LPCVD technique; Step S3 and Step D3: Deposition of Aluminum on the p-3C-SiC nanothin film and the underside of n-Si substrate; Step S4 and Step D4: Spin coating a photoresist layer on the surface of the p-3C-SiC nanothin film; Step S5 and Step D5: Photolithography process; Step S6 and Step D6: Wet etching of deposited Aluminum on the p-3C-SiC surface and removing the photoresist layer; Step S7 and Step D7: Dicing the samples from wafer; Step S8 and Step D8: p-3C-SiC/n-Si device and p-3C-SiC/p-Si/n-Si device, respectively.

forthcoming sections, a comprehensive experiment and theoretical analysis is conducted to demonstrate and explain the enhancement of the optoelectronic properties (e.g., vertical photocurrent and photoresponsivity) of the DJ structure compared to the SJ counterpart. The wafers were fabricated by a Japanese company specialized in semiconductor materials, and detailed technical specifications of the two wafers are provided in Table S1 (Supporting Information). Aluminum electrodes on the surfaces of p-3C-SiC and n-Si are employed for collecting photogenerated charge carriers. The electrode in the surface of the p-3C-SiC has dimensions of 200 μm × 1000 μm.

2.2. Fabrication of the Heterostructures. The SJ structure was fabricated by directly growing p-3C-SiC epilayers on an n-Si (100) wafer using low-pressure chemical vapor deposition (LPCVD) at approximately 1,100 °C. We extended this concept further to the fabrication of the double junction structure. The middle p-Si layer was also grown directly on the n-Si substrate by LPCVD. The p-3C-SiC layer was then grown directly on the middle p-Si layer. The doping concentration was measured using secondary ion mass spectrometry (SIMS) and resistivity measurements. The grown process was performed by a Japanese company D&X (details in Supporting Information). Figure 2 shows the fabrication process and the design of SJ and DJ devices from two wafers. This standard fabrication process for 3C-SiC/Si devices and all samples was implemented in the cleanroom of the **Queensland Micro Nanotechnology Centre—Griffith University**. To ensure the removal of residue, dirt, and surface oxides from the wafers, the two wafers were first cleaned with 4:1 piranha (a mixture of sulfuric acid-H_2SO_4 and hydrogen peroxide-H_2O_2) for approximately 15 min and then immersed in HF (1%) for 1 min. Next, the wafers were dried and covered with a 200 nm aluminum layer on top of the 3C-SiC nanofilm. We continued sputtering the aluminum layer on the other side of the silicon wafer (n-Si). Photoresist (AZ 1512) was spin coated at 3,500 rpm on the aluminum layer. The wavelength and exposure time used for photolithography were 405 nm and 30 min, respectively. The electrodes were patterned by standard photolithography and subsequently formed by wet etching. The material used in wet etching was $H_3PO_4:CH_3COOH:HNO_3 = 20:4:1$. Finally, the SJ and DJ devices were diced and separated from the wafer.

The wafer was annealed in two stages to create the ohmic contact between the aluminum electrodes and the semiconductors (p-3C-SiC nanothin film and n-Si substrate). First, the devices were annealed at 450 °C for 30 min in vacuum to ensure ohmic contact between aluminum and Si.[40] Subsequently, the annealing process was performed in dry nitrogen (N_2) at 600 °C for 4 min for the ohmic contact between aluminum and 3C-SiC.[29]

2.3. Characterization of Semiconductor Layers. We designed the carrier concentrations of the grown p-3C-SiC film and the n-Si substrate to be approximately 5×10^{18} and 10^{14} atoms/cm³, respectively, while the doping concentration of the p-type Si middle layer was 10^{16} atoms/cm³. The thicknesses of the p-3C-SiC and n-Si layers of both structures are **500 nm** and approximately **500 μm**, respectively. The thickness of the
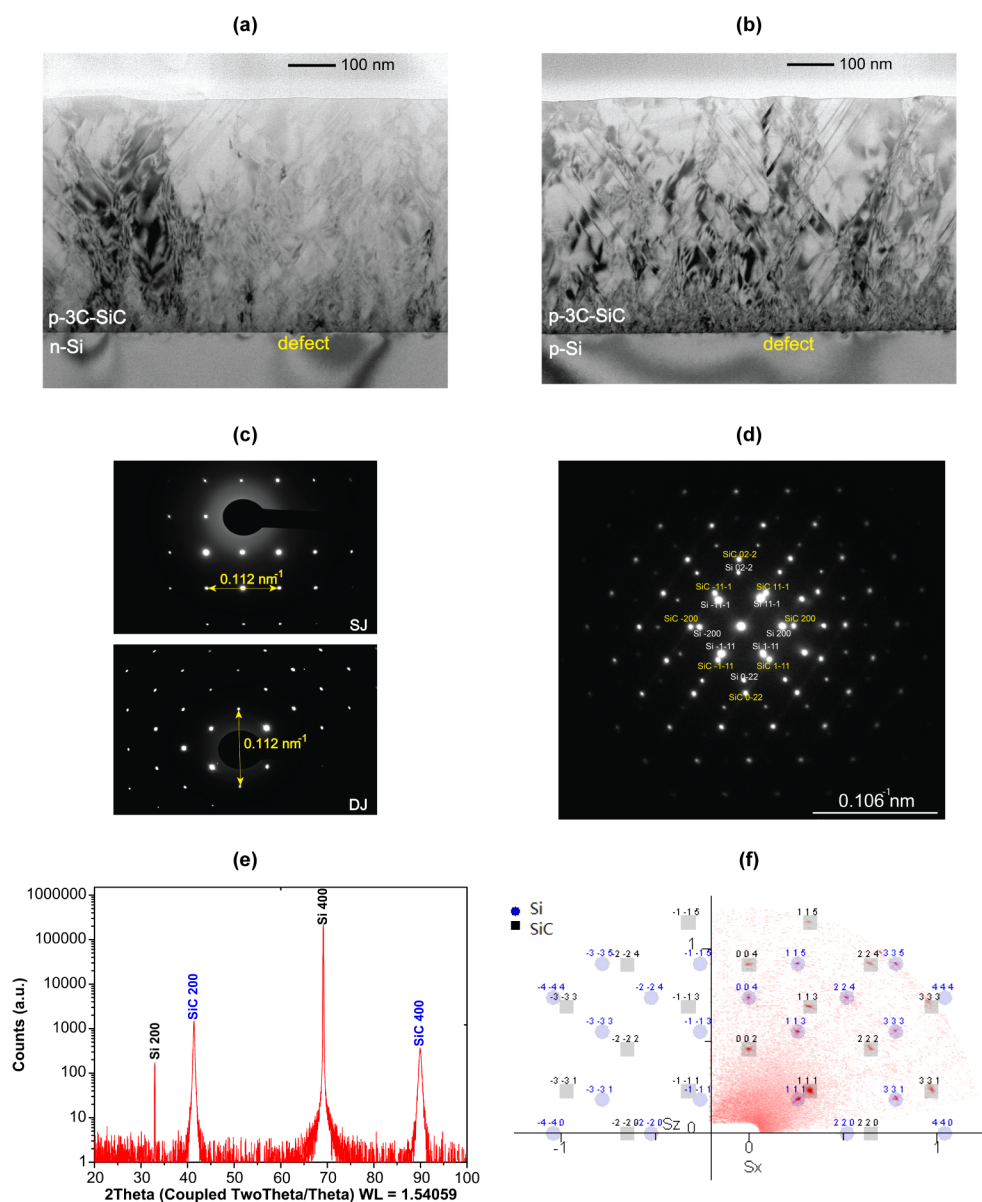
Figure 3. Material characterization and structural property of devices. (a) Transmission electron microscopy (TEM) image of p-3C-SiC/n-Si structure. (b) TEM image of p-3C-SiC/p-Si/n-Si structure. (c) SAED images of 3C-SiC nanothin films in SJ and DJ structures. (d) The SAED pattern at the SiC-Si boundary shows that the crystals are well aligned. (e) Symmetric X-ray diffraction (XRD) pattern of the grown 3C-SiC on a Si substrate. (f) Wide-range reciprocal space mappings of the grown 3C-SiC on p-Si/n-Si showing that SiC < 001> aligns perfectly with the Si < 001> crystal orientation, S = 1/d.

middle p-type-Si layer is **1 μm**. The dopant of the p-type 3C-SiC layer and p-type Si middle layer was boron, while the n-type Si substrate was doped with phosphorus. The process of fabricating the wafers was performed by the Japanese company D&X, and the specifications of p-3C-SiC/n-Si and p-3C-SiC/p-Si/n-Si are detailed in Table S1.

3. METHODS

3.1. Material Characterization and Structural Property. Next, the material characterization of the two heterostructures is conducted to confirm the physical and chemical properties of the two heterostructures. Figure 3 illustrates the material characterization and structural properties including transmission electron microscopy (TEM), selected area electron diffraction (SAED), single crystal X-ray diffraction (XRD) measurement, and wide-range reciprocal

space mapping (WRSM). The high-resolution TEM images of the SJ and DJ structures are shown in Figures 3a and b, respectively. The high-resolution TEM images evidently show lattice fringes with very few defect atoms, reflecting that the grown cubic 3C-SiC is well crystallized with Si. High-quality SiC can be achieved from a distance of approximately 50 nm from the interface. The cross-sectional Scanning Electron Microscopy (SEM) images (Figure S1) also clearly reveal the homogeneous 3C-SiC layer with a thickness of ∼500 nm grown on top of the Si substrate. Figure 3c shows the SAED patterns of the grown 3C-SiC nanothin film of the SJ and DJ structures. The SAED pattern taken from the [011] axis clearly shows a single crystalline 3C-SiC layer with a cubic structure. Additional information regarding the crystal growth orientation of 3C-SiC on a Si substrate, especially within the area where these two crystal lattices intersect, is provided in Figure
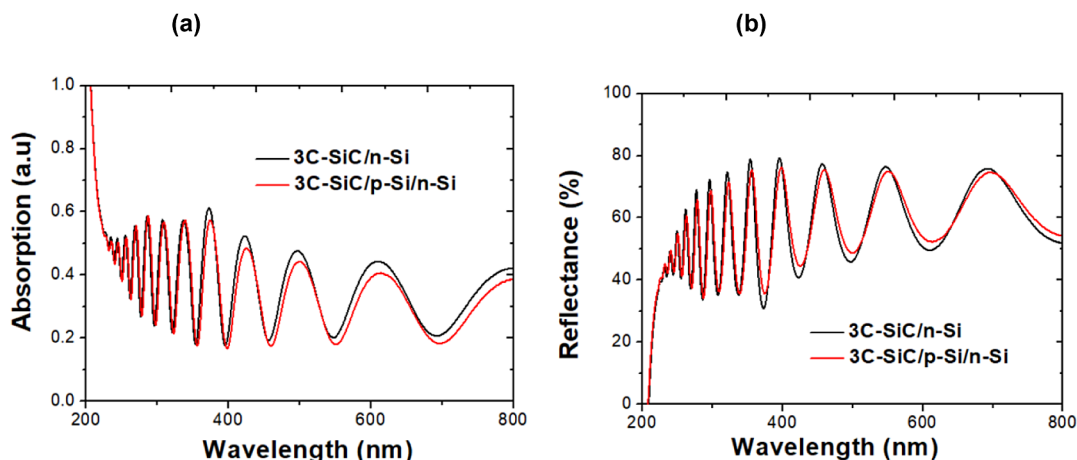
Figure 4. Absorption (a) and reflectance (b) spectrum of the SJ and DJ heterostructures.
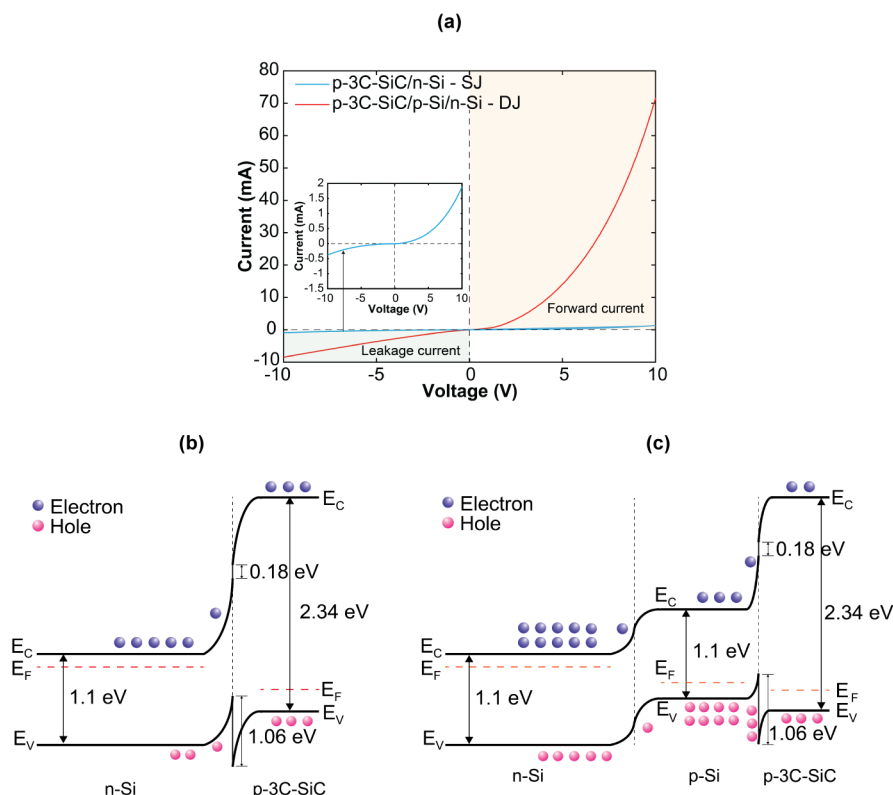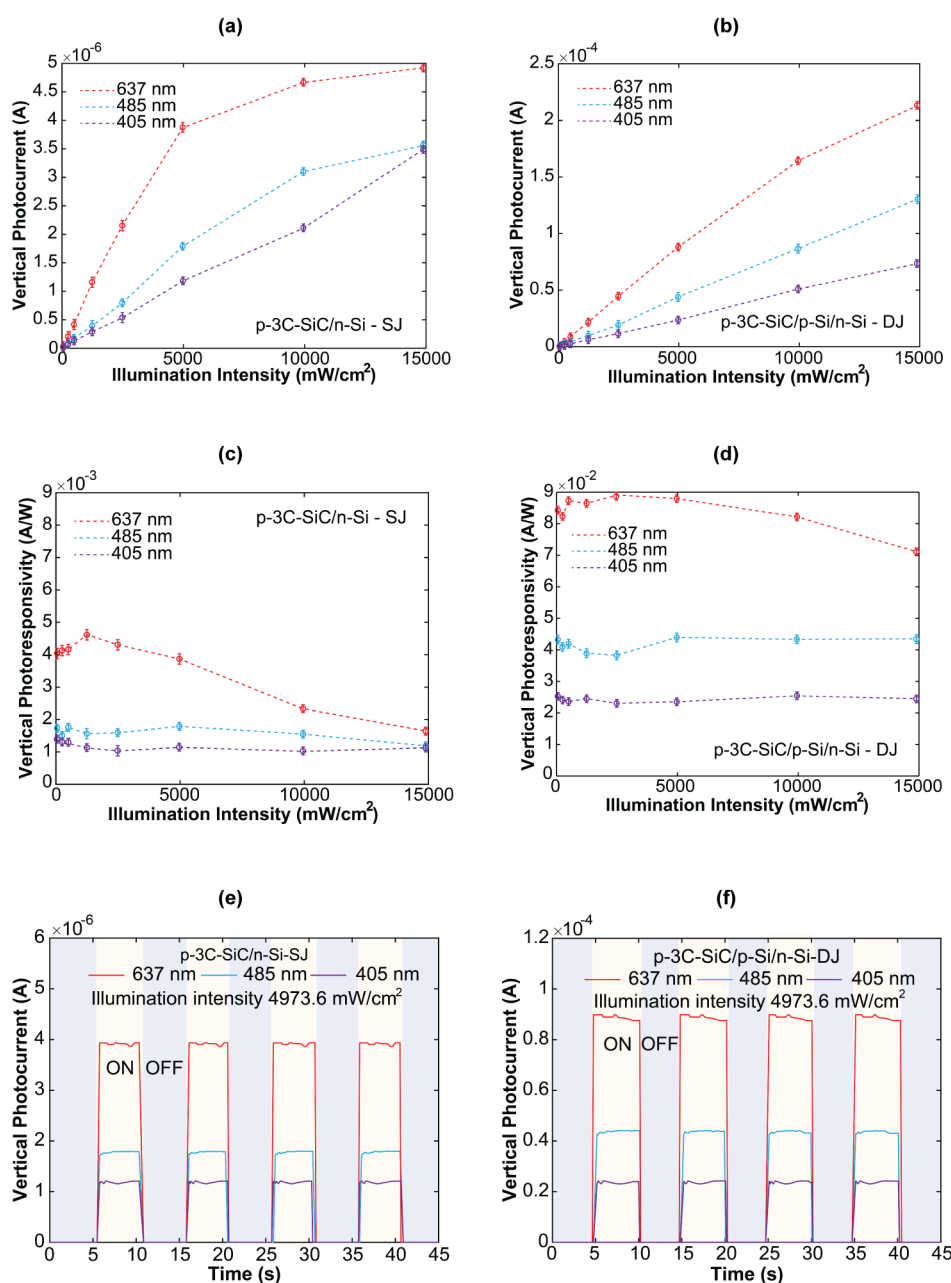

Figure 5. Electronic characteristic of devices. (a) Current−voltage (I−V) curve in dark condition; (b) energy band diagram of SJ structure under forward bias of I−V measurement in dark condition; (c) energy band diagram of DJ structure under forward bias of I−V measurement in dark condition.

3d. The diffraction pattern confirms that SiC(02−2), SiC(11−1), SiC(200), SiC(1−11), SiC(0−22), SiC(−1−11), SiC(−200), and SiC(−111) all aligned well with the corresponding orientation of the Si substrate. TEM and SAED images were captured using a Hitachi HT 7700 microscope equipped with a tungsten filament and operated at 100 kV.

The orientation of the film was subsequently characterized by single crystal XRD measurements, as shown in Figure 3e. The symmetric X-ray diffraction pattern of the grown 3C-SiC on Si substrate can match the standard XRD pattern of Si and Si Moissanite 3C, with the obtained pattern exhibiting XRD peaks at 41.4°, 90.1° and 69.2° corresponding to 3C-SiC(200),

3C-SiC(400), and Si(400), respectively. This result confirms the aligned orientation of the single crystal of p-3C-SiC grown on Si. We further determined a wide-range reciprocal space mapping of the 3C-SiC/Si sample in Figure 3f, which clearly shows that SiC and Si align perfectly along the (001) orientation with favorable crystallinity.

Wide-range reciprocal space mapping procedure was employed in the investigation of an epitaxial SiC layer grown on a Si substrate. The alignment of the SiC layer on the Si substrate was achieved by positioning it on an RxRy attachment head situated on the φ stage of a Rigaku SmartLab diffractometer. The instrument was operated under CuKα1 radiation. On the primary side, a CBO Parallel Beam Mirror

Figure 6. Vertical optoelectronic characteristics of SJ and DJ devices. (a) and (b) Vertical photocurrent of the SJ and DJ devices, respectively. (c) and (d) Vertical photoresponsivity of the SJ and DJ devices, respectively. (e) and (f) Time-dependent photoresponse of the SJ and DJ devices at three wavelengths with an illumination intensity of 4973.6 mW/cm².

followed by a Ge(220 × 2) two-bounce monochromator was equipped. Preceding the Hypix3000 detector in 0D mode, an assortment of optical components, including a motorized antiscattering slit and a 5° axial Soller slit, were employed.

Offset Theta/2Theta scans were conducted along both the Si 001 and Si 311 directions to elucidate the crystal orientation between the SiC layer and the Si template. This led to the successful recording of reciprocal space mapping data for Si/SiC 004, Si/SiC $3\bar{1}\bar{1}$, and Si/SiC 511. Subsequently, a comprehensive wide-range reciprocal space mapping across the entire measurable reciprocal space was executed to investigate the relationship between the SiC layer and the Si substrate. For this task, the sample was positioned on a $\chi-\varphi$ cradle. The optical setup included a primary point focus beam configuration comprising a CBO-PB 0.5 mm pinhole, a CBO-f

polycapillary module, and a long collimator with a 0.8 mm diameter. A Hypix3000 detector was strategically placed at a distance of 121 mm from the sample to capture 2D diffraction frames, facilitating subsequent "Chi-expansion" merging in Rigaku 2PD software and visualization in 3DE software.

X-ray photoelectron spectroscopy (XPS) analysis was carried out using the Thermo Scientific Al K-Alpha XPS system, with energy steps of 0.1 eV employed in the data acquisition process.

3.2. Optical Properties of the Devices. Figure 4 shows the absorption and reflectance spectrum of SJ and DJ structures as a function of wavelength. The optical characteristics in the UV–visible wavelength of both structures exhibit notable similarities. The strong interference fringe effect is

Table 1. Optoelectronic Performance Comparisons of Vertical Self-Powered SJ and DJ Devices at 2487 mW/cm² (λ = 637 nm)[a]

Device structure	I_{dark} [A]	Photoresponsivity [mA/W]	Rise time [s]	Fall time [s]	Detectivity ×10¹⁰ [Jones]	EQE [%]
p-3C-SiC/n-Si - SJ	5.55×10^{-10}	$(4.300 \pm 0.006)*$	0.521	0.507	(0.4575 ± 0.0006)	(0.840 ± 0.001)
p-3C-SiC/p-Si/n-Si - DJ	9.81×10^{-9}	$(88.25 \pm 0.48)*$	0.412	0.262	(2.233 ± 0.010)	(17.179 ± 0.093)

[a]*Average values and standard deviation obtained from measurements of 5 devices.

observed in the optical spectrum indicating the high uniformity of both films.

The optical measurements were done using a Cary 5000 UV−vis-NIR Spectrophotometer (Agilent).

3.3. Electronic Characteristics. To characterize the electrical properties in both devices, the two electrodes on the top and bottom are wired externally for voltage sweeping (−10 to +10 V) to measure the current−voltage (I−V) curves under dark conditions. Figure 5a describes the diode characteristics of the SJ and DJ devices, including the nonlinear curves of the forward and leakage currents. Based on the graph, the current in the DJ device is much larger than the current in the SJ device at the same voltage. This phenomenon is explained as follows.[32,33] According to the energy band diagrams depicted in Figures 5c,d for SJ and DJ structures, holes face energetic challenges when attempting to surmount the energy barrier between regions p-3C-SiC and n-Si (in the SJ structure) and between p-3C-SiC and p-Si (in the DJ structure) under forward bias conditions. This difficulty arises from the fact that the valence band energy levels of n-Si and p-Si are both positioned higher than that of p-3C-SiC. The energy band diagrams for all layers in both structures were determined using ultraviolet photoelectron spectroscopy (UPS), as detailed in Figure S4 of the Supporting Information. As a consequence, there is a greater likelihood of recombination current occurring within heterojunctions. However, in a double junction (DJ) device, charge carriers originating from the homojunction (p-Si/n-Si junction) exert a forceful influence, effectively propelling the struggling holes at the heterojunction (p-3C-SiC/p-Si junction) toward the upper electrode once the external bias voltage surpasses 3 V. This situation results in a reduction in series resistance (R_s) and an accompanying increase in current within this forward region. Such a phenomenon is absent in the single junction (SJ) structure, which explains the significantly higher current observed in the DJ structure in the linear portion of the forward region. The current density is mathematically calculated as follows:[32]

$$J = J_0[e^{[\frac{q(V-JR_s)}{nK_BT}]} - 1] + J_{sh} - J_{ph} \tag{1}$$

where J_0 is the reverse bias saturation current density; q is the elementary charge; R_s is the series resistance; n is the ideality factor; K_B is Boltzmann's constant; T is the temperature; $J_{sh} = \frac{V - JR_s}{R_{sh}}$ is the shunt current; R_{sh} is the shunt resistance; and J_{ph} is the photocurrent. Shunt current signifies the device leakages responsible for the parasitic current that flows directly from one electrode to another. In essence, the term represents

an undesirable factor that impairs the performance of a photodetector.

Another rationale for the higher current in the DJ structure compared to the SJ structure can be attributed to the substantial heat generated as the external voltage increases. It is well established that heat is directly proportional to the square of the current or voltage, resulting in considerable heat generation within these structures. In DJ devices, the presence of two junctions leads to the generation of a greater number of electron-hole pairs, which subsequently migrate more efficiently toward the electrodes under the influence of the forward bias region.

## 4. RESULTS AND DISCUSSION

4.1. Enhancement of the Photocurrent and Photoresponsivity in the DJ Structure. The experimental setup for vertical optoelectronic characterization of both devices is shown in Figure S2. Figures 6a and b and Tables S2a,b show the photocurrents ($I_{ph} = I_{light} - I_{dark}$) under laser illumination at different wavelengths of 637, 485, and 405 nm. We observed that I_{ph} increases with increasing illumination intensity as more charge carriers are generated. According to these results, the DJ structure shows superiority in converting photoenergy to electrical energy compared to the SJ structure. The vertical photocurrents in the DJ device were much higher (from 18.11 to 43.33 times) than those in the SJ device. The enhancement of the photocurrent in the DJ structure is due to the bijunction structure with a higher carrier concentration and longer carrier lifetime.[5,34] In addition, another possible reason for the enhancement is the mobility of electrons and holes in Si. The electron and hole mobilities in Si are 1,350 and 480 (cm²V⁻¹s⁻¹), respectively, which are much higher than 900 and 40 (cm²V⁻¹s⁻¹) as respectively observed in 3C-SiC.[35] The holes in the DJ device diffuse faster in the middle p-Si layer, forming multiple streams of charge carriers moving up the p-3C-SiC layer, thereby creating a large vertical photocurrent (Figure 1b). This phenomenon presents the great potential of the p-3C-SiC/p-Si/n-Si structure in sensing and energy-harvesting applications. This unique feature is also regarded as the key to new designs for other semiconductor materials with DJ structures to achieve much higher photoelectric energy conversions than SJ structures.

A photodetector's performance may be evaluated using its vertical photoresponsivity (R) at a specific wavelength, which is defined:[37]

$$R = \frac{I_{ph}}{P \times S} \tag{2}$$

where R is the vertical photoresponsivity (A/W); I_{ph} is the vertical photocurrent (A); P is the incident optical power on
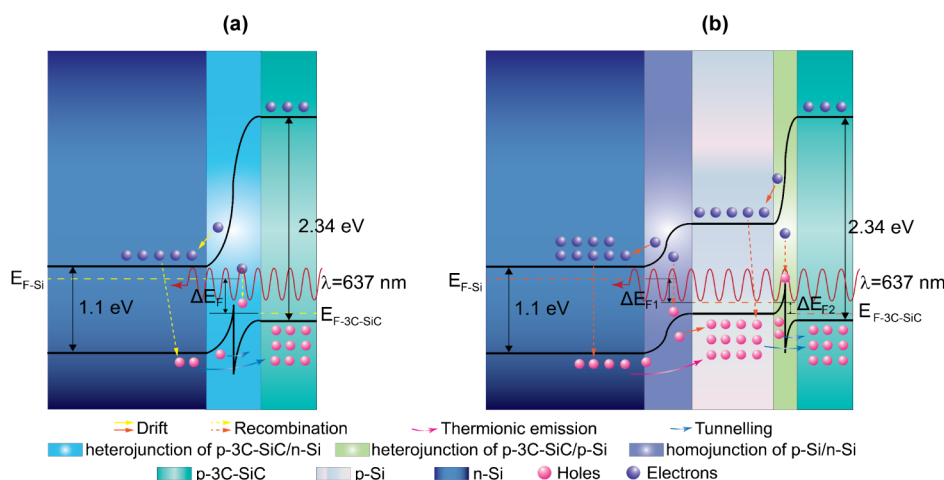
Figure 7. Energy band diagrams and generation and transport of charge carriers for two devices under laser lights. (a) and (b) Energy band diagrams of SJ and DJ devices at 637 nm, respectively.

the effective area (W/cm^2); and S is the illuminated area (cm^2). Figures 6c and d show the vertical photoresponsivity of the two devices at different illumination intensities of laser light. The vertical photoresponsivity peaked at 4.62×10^{-3} A/W with an illumination intensity of 1.24×10^3 mW/cm^2 (at λ = 637 nm) for p-3C-SiC/n-Si and 8.91×10^{-2} A/W at an illumination intensity of 2.487×10^3 mW/cm^2 for p-3C-SiC/p-Si/n-Si. The low reflectance also explains this phenomenon by scattering at low intensity, resulting in a better photoelectric conversion efficiency at lower intensities than at higher levels.[37] Figures 6e and f describe the VPC repeatability of the SJ and DJ devices, respectively, when the laser light is periodically turned on and off at three wavelengths (637, 485, and 405 nm) with an illumination intensity of 4973.6 mW/cm^2. The device has good repeatability at three wavelengths, and the VPC of the red laser (637 nm) is highest. In addition, the VPCs of the DJ device at three wavelengths of 637, 485, and 405 nm are approximately 22, 24, and 20 times higher than that of the SJ device, respectively. Additionally, Figure S3 shows the reliability and reproducibility of both devices after a period of approximately 15 days.

Table 1 compares the optoelectronic performance of the SJ and DJ devices at a wavelength of 637 nm. The SJ device demonstrates a vertical photoresponsivity of 4.3×10^{-3} (A/W) and a detectivity of 0.46×10^{10} (Jones), whereas the DJ device surpasses these figures with a superior photoresponsivity of 8.83×10^{-2} (A/W) and a detectivity of 2.23×10^{10} (Jones).

The external quantum efficiency (EQE) is calculated as follows:[36]

$$EQE = \frac{R_\lambda}{\lambda} \times \frac{hc}{e} \approx \frac{R_\lambda}{\lambda} \times \left(1240W\frac{nm}{A}\right) \quad (3)$$

where R_λ is the photoresponsivity (A/W) with a certain wavelength, λ is the wavelength (nm), h is the Plank constant, c is the speed of light, and e is the elementary charge.[36] The EQE values for the SJ and DJ devices were determined to be 0.84% and 17.3%, respectively. This represents a remarkable enhancement of more than 20-fold in EQE achieved with the DJ device.

Table S3 presents the photoresponsivity, EQE, and detectivity of the two heterostructures at three different wavelengths at an irradiance power of 2487 mW/cm^2. It is evident from the data that the DJ structure outperforms the SJ

structure significantly, highlighting the promising potential of DJ-based device in enhancing photodetection characteristics.

Furthermore, Table S4 provides a comparative analysis of performance parameters for self-powered photodetectors. The superiority of the DJ structure in terms of photoresponsivity is distinctly evident from the data presented in this table.

4.2. Underlying Physics Mechanism. When exposed to laser light, electron-hole (e-h) pairs in the device are predominantly generated at the junctions, with some additional generation in the p-Si layer for the DJ device and in the n-Si layer for both devices. These excited electrons migrate from the valence band to the conduction band, thereby leaving free holes in the valence band. These holes subsequently move to the p-3C-SiC nanothin film, while the electrons descend to the lower layer in the SJ device, as depicted in Figure 1a. The physical mechanism in the DJ device remains consistent. However, there are some differences that lead to the superior performance of the DJ device compared to its SJ counterpart. Upon exposure to illumination, e-h pairs are formed at junction 1 (between p-3C-SiC and p-Si) and junction 2 (between p-Si and n-Si). Furthermore, a distinct population of e-h pairs is generated in the vicinity of junction 2 in the n-Si region and in the vicinity of junction 1 in the p-Si region. The generated holes migrate upward through the p-3C-SiC layer, while the electrons exhibit a tendency to move downward. Therefore, the DJ photodetector exhibits a greater photocurrent in comparison to the SJ device, attributable to its bijunction structure and higher carrier concentration, as illustrated in Figure 1b. The number of generated photocarriers can be calculated as follows:[38,39]

$$n = \frac{\mu P \tau}{\left(\frac{1}{\alpha}\right)Ah\nu} \quad (4)$$

where n is the generated photocarrier; μ is the quantum efficiency; P is the incident optical power; τ is the carrier lifetime; $\frac{1}{\alpha}$ is the light penetration depth; A is the illuminated area; and $h\nu$ is the photon energy.

Equation 4 indicates that the generated photocarriers n of the DJ device are much higher than those of the SJ device due to parameters such as μ and τ. The quantum efficiency, which is defined as the number of carriers generated per photon, is higher in the DJ structure owing to the increased quantity of

charge carriers generated. The carrier lifetime in the DJ is also longer because the holes can reach the diffusion region before recombining.[34] Two internal electric fields of the DJ structure also help to prevent any recombination of generated e-h pairs.[34] In addition, the width of the depletion regions between the p-3C-SiC and p-Si layers is also narrower than that of p-Si and n-Si, resulting in further improvement of the photocurrent.[5]

To elucidate the e-h pair generation and charge carrier transport mechanism of SJ and DJ devices, a schematic bandgap diagram was drawn under three wavelengths of 637, 485, and 405 nm, as shown in Figures 7a,b, Figures S5a,b, and S5c,d, respectively. First, the energy band diagrams of each semiconductor layer were measured by ultraviolet photoelectron spectroscopy (UPS), as indicated in Figure S4. For 637 nm laser illumination, the incident photons transmit through the p-3C-SiC layer and are mainly absorbed in the n-Si layer for the SJ device. Moreover, these photons pass through the p-3C-SiC layer and are mainly absorbed in the middle p-Si layer and partly in the n-Si layer of the DJ device. Here, e-h pairs are generated at the junctions, p-3C-SiC and n-Si (for the SJ device) and p-Si and n-Si (for the DJ device). For shorter wavelengths, most incident photons will be absorbed by the p-3C-SiC layer, and only part of the light will reach the Si bottom layers. This dynamic results in low efficiency of converting light to electrical energy, such that extra light energy is dissipated as heat inside these devices.[38,39] This dissipation explains why with the same laser power per unit area, the vertical photocurrent of the longer wavelength is higher than that of the shorter wavelength. Under light excitation, the electrons and holes have different states. The holes migrate to the p-3C-SiC layer by the tunneling mechanism at the layer of junctions (p-3C-SiC and n-Si; p-3C-SiC and p-Si) or by thermionic emission from the n-Si layer to the p-Si. However, they can also be recombined with nearby electrons. In addition, for the heterojunction between p-3C-SiC and p-Si, the holes migrate to the p-3C-SiC layer by the tunneling effect since the work function of these two layers is small and the E_v of the p-Si layer is smaller than that of p-3C-SiC.

5. CONCLUSION

The present study demonstrates the superior performance of vertical optoelectronic devices made with the monolithic integration of p-3C-SiC/p-Si/n-Si double junctions compared to the p-3C-SiC/n-Si single heterojunction when operating in a self-power mode. The designed DJ device achieved an outstanding vertical photoresponsivity of more than 43 times that of the SJ device at 14 921 mW/cm^2 (λ = 637 nm). In addition, the highest photoresponsivity, rise time and fall time, detectivity and EQE of the DJ device were superior to those of the SJ device. The middle p-Si layer plays a crucial role in the performance of the design, as its hole mobility is significantly higher than that of the p-3C-SiC layer. This configuration leads to the formation of large flows of charge carriers that can reach the p-3C-SiC layer, resulting in both high vertical photocurrent and vertical photoresponsivity. The principles of generated and diffused charge carriers are invoked to explain the migration of both holes and electrons under the influence of excited light. Energy band diagrams identify the distinct light absorption mechanisms of the structures at different wavelengths. We successfully and consistently fabricated our optoelectronic devices, demonstrating their great potential in advancing

sensing, energy harvesting applications, as well as mechatronics engineering.

■ ASSOCIATED CONTENT

Data Availability Statement

The data that support the plots within this paper and the other findings of this study are available from the corresponding authors upon reasonable request.

ⓢ Supporting Information

The Supporting Information is available free of charge at https://pubs.acs.org/doi/10.1021/acsami.4c03875.

> Specifications of p-3C-SiC/n-Si and p-3C-SiC/p-Si/n-Si; SEM images of cross-sections of SJ and DJ heterostructures; experimental setup for vertical optoelectronic characteristics of the devices; vertical photocurrent of SJ and DJ devices with different laser powers and wavelengths; repeatability of photoresponse of the SJ and DJ devices at 637 nm wavelength with an illumination intensity of 4973.6 mW/cm^2; the responsivity, quantum efficiency, and detectivity of the photodetector at different wavelengths; comparative analysis of performance parameters for self-powered photodetectors under zero bias; ultraviolet photoelectron spectroscopy (UPS) and energy band diagrams; energy band diagrams and generation and transport of charge carriers for two devices under laser wavelengths of 485 and 405 nm (PDF)

■ AUTHOR INFORMATION

Corresponding Author

Dinh Gia Ninh − Queensland Micro and Nanotechnology Centre (QMNC), Griffith University, Brisbane, QLD 4111, Australia; School of Engineering and Built Environment, Griffith University, Gold Coast, QLD 4215, Australia; Group of Materials and Structures, Hanoi University of Science and Technology, Hanoi 100000, Vietnam; ⓞ orcid.org/0000-0002-9903-8847; Email: ninh.dinh@griffithuni.edu.au, ninh.dinhgia@hust.edu.vn

Authors

Minh Tam Hoang − School of Chemistry and Physics, Faculty of Science, Queensland University of Technology, Brisbane, QLD 4001, Australia; Centre for Materials Science, Queensland University of Technology (QUT), Brisbane, QLD 4001, Australia

Tuan-Hung Nguyen − Queensland Micro and Nanotechnology Centre (QMNC), Griffith University, Brisbane, QLD 4111, Australia; ⓞ orcid.org/0000-0003-3388-9654

Erik Streed − Institute for Glycomics, Griffith University, Southport 4222, Australia

Sima Dimitrijev − Queensland Micro and Nanotechnology Centre (QMNC), Griffith University, Brisbane, QLD 4111, Australia

Philip Tanner − Queensland Micro and Nanotechnology Centre (QMNC), Griffith University, Brisbane, QLD 4111, Australia

Tuan-Khoa Nguyen − Queensland Micro and Nanotechnology Centre (QMNC), Griffith University, Brisbane, QLD 4111, Australia; ⓞ orcid.org/0000-0003-1271-9576

Nam-Trung Nguyen − *Queensland Micro and Nanotechnology Centre (QMNC), Griffith University, Brisbane, QLD 4111, Australia*

Hongxia Wang − *School of Chemistry and Physics, Faculty of Science, Queensland University of Technology, Brisbane, QLD 4001, Australia; Centre for Materials Science, Queensland University of Technology (QUT), Brisbane, QLD 4001, Australia;* ⊙ orcid.org/0000-0003-0146-5259

Yong Zhu − *School of Engineering and Built Environment, Griffith University, Gold Coast, QLD 4215, Australia*

Van Dau − *School of Engineering and Built Environment, Griffith University, Gold Coast, QLD 4215, Australia*

Dzung Viet Dao − *Queensland Micro and Nanotechnology Centre (QMNC), Griffith University, Brisbane, QLD 4111, Australia; School of Engineering and Built Environment, Griffith University, Gold Coast, QLD 4215, Australia;* ⊙ orcid.org/0000-0002-6348-0879

Complete contact information is available at:
https://pubs.acs.org/10.1021/acsami.4c03875

Author Contributions

D.G.N. contributed to conceptualization, fabrication, investigation, methodology, formal analysis, data curation, validation, writing—original draft, writing—review and editing. M.T.H. contributed to investigation, formal analysis, data curation, writing—original draft. T.-H.N. contributed to investigation, formal analysis, writing—review and editing. E.S. contributed to resources, formal analysis, writing—review and editing. S. contributed to formal analysis, writing—review and editing. P.T. contributed to fabrication, formal analysis, writing—review and editing. T.-K. N. contributed to fabrication, formal analysis, writing—review and editing. N.-T.N. contributed to supervision, resources, writing—review and editing. H.W. contributed to supervision, resources, writing—review and editing. Y.Z. contributed to supervision, writing—review and editing. V.D. contributed to supervision, project administration, writing—review and editing. D.V.D. contributed to investigation, conceptualization, methodology, supervision, project administration, writing—review and editing. All authors read and commented on the paper.

Notes

The authors declare no competing financial interest.

■ REFERENCES

(1) Essig, S.; Allebé, C.; Remo, T.; Geisz, J. F.; Steiner, M. A.; Horowitz, K.; Barraud, L.; Ward, J. S.; Schnabel, M.; Descoeudres, A.; Young, D. L.; Woodhouse, M.; Despeisse, M.; Ballif, C.; Tamboli, A. Raising the one-sun conversion efficiency of III−V/Si solar cells to 32.8% for two junctions and 35.9% for three junctions. *Nat. Energy* **2017**, *2* (9), 17144.

(2) Shen, P.; Cao, F.; Wang, H.; Wei, B.; Wang, F.; Sun, X. W.; Yang, X. Solution-Processed Double-Junction Quantum-Dot Light-Emitting Diodes with an EQE of over 40%. *ACS Appl. Mater. Interfaces* **2018**, *11* (1), 1065−1070.

(3) Guo, F.; Li, N.; Fecher, F. W.; Gasparini, N.; Quiroz, C. O. R.; Bronnbauer, C.; Hou, Y.; Radmilović, V. V.; Radmilović, V. R.; Spiecker, E.; Forberich, K.; Brabec, C. J. A Generic Concept to Overcome Bandgap Limitations for Designing Highly Efficient Multi-Junction Photovoltaic Cells. *Nat. Commun.* **2015**, *6* (1), 7730.

(4) Torabi, N.; Behjat, A.; Zhou, Y.; Docampo, P.; Stoddard, R. J.; Hillhouse, H. W.; Ameri, T. Progress and Challenges in Perovskite Photovoltaics from Single- to Multi-Junction Cells. *Mater. Today Energy* **2019**, *12*, 70−94.

(5) Luo, Z.; Yang, M.; Wu, D.; Huang, Z.; Gao, W.; Zhang, M.; Zhou, Y.; Zhao, Y.; Zheng, Z.; Li, J. Rational Design of WSe_2 /WS_2 /WSe_2 Dual Junction Phototransistor Incorporating High Responsivity and Detectivity. *Small Methods* **2022**, *6* (9), 2200583.

(6) Yamaguchi, M.; Dimroth, F.; Geisz, J. F.; Ekins-Daukes, N. J. Multi-Junction Solar Cells Paving the Way for Super High-Efficiency. *J. Appl. Phys.* **2021**, *129* (24), 240901.

(7) Philipps, S. P.; Bett, A. W. III-V Multi-Junction Solar Cells and Concentrating Photovoltaic (CPV) Systems. *Adv. Opt. Technol.* **2014**, *3* (5−6), 469−478.

(8) Li, Z.; Hong, E.; Zhang, X.; Deng, M.; Fang, X. Perovskite-Type 2D Materials for High-Performance Photodetectors. *J. Phys. Chem. Lett.* **2022**, *13* (5), 1215−1225.

(9) Chen, D.-R.; Hofmann, M.; Yao, H.-M.; Chiu, S.-K.; Chen, S.-H.; Luo, Y.-R.; Hsu, C.-C.; Hsieh, Y.-P. Lateral Two-Dimensional Material Heterojunction Photodetectors with Ultrahigh Speed and Detectivity. *ACS Appl. Mater. Interfaces* **2019**, *11* (6), 6384−6388.

(10) Han, L.; Peng, M.; Wen, Z.; Liu, Y.; Zhang, Y.; Zhu, Q.; Lei, H.; Liu, S.; Zheng, L.; Sun, X.; et al. Self-Driven Photodetection Based on Impedance Matching Effect between a Triboelectric Nano-generator and a MoS2 Nanosheets Photodetector. *Nano Energy* **2019**, *59*, 492−499.

(11) Yan, F.; Wei, Z.; Wei, X.; Lv, L.; Zhu, W.-K.; Wang, K. Toward High-Performance Photodetectors Based on 2D Materials: Strategy on Methods. *Small Methods* **2018**, *2* (5), 1700349.

(12) Huang, Z.; Liu, J.; Zhang, T.; Jin, Y.; Wang, J.; Fan, S.; Li, Q. Interfacial Gated Graphene Photodetector with Broadband Response. *ACS Appl. Mater. Interfaces* **2021**, *13* (19), 22796−22805.

(13) Chen, Z.; Li, X.; Wang, J.; Tao, L.; Long, M.; Liang, S.-J.; Lay, K. A.; Shu, C.; Tsang, H. K.; Xu, J.-B. Synergistic Effects of Plasmonics and Electron Trapping in Graphene Short-Wave Infrared Photodetectors with Ultrahigh Responsivity. *ACS Nano* **2017**, *11* (1), 430−437.

(14) Zhao, M.; Xue, Z.; Zhu, W.; Wang, G.; Tang, S.; Liu, Z.; Guo, Q.; Chen, D.; Chu, P. K.; Ding, G.; et al. Interface Engineering-Assisted 3D-Graphene/Germanium Heterojunction for High-Performance Photodetectors. *ACS Appl. Mater. Interfaces* **2020**, *12* (13), 15606−15614.

(15) Sun, Z.; Chang, H. Graphene and Graphene-like Two-Dimensional Materials in Photodetection: Mechanisms and Methodology. *ACS Nano* **2014**, *8* (5), 4133−4156.

(16) Li, J.; Yuan, S.; Tang, G.; Li, G.; Liu, D.; Li, J.; Hu, X.; Liu, Y.; Li, J.; Yang, Z.; Liu, S. F.; Liu, Z.; Gao, F.; Yan, F. High-Performance, Self-Powered Photodetectors Based on Perovskite and Graphene. *ACS Appl. Mater. Interfaces* **2017**, *9* (49), 42779−42787.

(17) Asuo, I. M.; Fourmont, P.; Ka, I.; Gedamu, D.; Bouzidi, S.; Pignolet, A.; Nechache, R.; Cloutier, S. G. Highly Efficient and Ultrasensitive Large-Area Flexible Photodetector Based on Perovskite Nanowires. *Small* **2018**, *15* (1), 1804150.

(18) Li, S.-X.; Xia, H.; Sun, X.-C.; An, Y.; Zhu, H.; Sun, H.-B. Curved Photodetectors Based on Perovskite Microwire Arrays via in Situ Conformal Nanoimprinting. *Adv. Funct. Mater.* **2022**, *32*, 29.

(19) Wang, Y.; Song, L.; Chen, Y.; Huang, W. Emerging New-Generation Photodetectors Based on Low-Dimensional Halide Perovskites. *ACS Photonics* **2020**, *7* (1), 10−28.

(20) Patel, M.; Pataniya, P. M.; Patel, V.; Sumesh, C. K.; Late, D. J. Large Area, Broadband and Highly Sensitive Photodetector Based on ZnO-WS2/Si Heterojunction. *Sol. Energy* **2020**, *206*, 974−982.

(21) Han, D.; Liu, K.; Chen, X.; Li, B.; Zhai, T.; Liu, L.; Shen, D. Performance Enhancement of a Self-Powered Solar-Blind UV Photodetector Based on ZnGa$_2$O$_4$/Si Heterojunction via Interface Pyroelectric Effect. *Appl. Phys. Lett.* **2021**, *118* (25), 251101.

(22) Pelella, A.; Grillo, A.; Faella, E.; Luongo, G.; Askari, M. B.; Bartolomeo, A. D. Graphene−Silicon Device for Visible and Infrared Photodetection. *ACS Appl. Mater. Interfaces* **2021**, *13* (40), 47895−47903.

(23) Li, G.; Liu, L.; Wu, G.; Chen, W.; Qin, S.; Wang, Y.; Zhang, T. Self-Powered UV-near Infrared Photodetector Based on Reduced Graphene Oxide/N-Si Vertical Heterojunction. *Small* **2016**, *12* (36), 5019−5026.

(24) Ji, T.; Liu, Q.; Zou, R.; Sun, Y.; Xu, K.; Sang, L.; Liao, M.; Koide, Y.; Yu, L.; Hu, J. An Interface Engineered Multicolor Photodetector Based on N-Si(111)/TiO$_2$ Nanorod Array Heterojunction. *Adv. Funct. Mater.* **2016**, *26* (9), 1400−1410.

(25) Wu, D.; Lou, Z.; Wang, Y.; Yao, Z.; Xu, T.; Shi, Z.; Xu, J.; Tian, Y.; Li, X.; Tsang, Y. H. Photovoltaic High-Performance Broadband Photodetector Based on MoS2/Si Nanowire Array Heterojunction. *Sol. Energy Mater. Sol. Cells* **2018**, *182*, 272−280.

(26) Zhang, Y.; Yu, Y.; Mi, L.; Wang, H.; Zhu, Z.; Wu, Q.; Zhang, Y.; Jiang, Y. In Situ Fabrication of Vertical Multilayered MoS$_2$/Si Homotype Heterojunction for High-Speed Visible-Near-Infrared Photodetectors. *Small* **2016**, *12* (8), 1062−1071.

(27) Mauthe, S.; Baumgartner, Y.; Sousa, M.; Ding, Q.; Rossell, M. D.; Schenk, A.; Czornomaz, L.; Moselund, K. E. High-speed III-V nanowire photodetector monolithically integrated on Si. *Nat. Commun.* **2020**, *11* (1), 4565.

(28) Mehregany, M.; Zorman, C. A. SiC MEMS: Opportunities and Challenges for Applications in Harsh Environments. *Thin Solid Films* **1999**, *355−356*, 518−524.

(29) Tanner, P.; Iacopi, A.; Phan, H.-P.; Dimitrijev, S.; Hold, L.; Chaik, K.; Walker, G. B.; Dao, V. D.; Nguyen, N.-T. Excellent Rectifying Properties of the N-3C-SiC/P-Si Heterojunction Subjected to High Temperature Annealing for Electronics, MEMS, and LED Applications. *Sci. Rep.* **2017**, *7* (1), 1−11.

(30) Senesky, D. G.; Jamshidi, B.; Bun Cheng, B. C.; Pisano, A. P. Harsh Environment Silicon Carbide Sensors for Health and Performance Monitoring of Aerospace Systems: A Review. *IEEE Sensors J.* **2009**, *9* (11), 1472−1478.

(31) Phan, H.-P.; Dao, V. D.; Nakamura, K.; Dimitrijev, S.; Nguyen, N.-T. The Piezoresistive Effect of SiC for MEMS Sensors at High Temperatures: A Review. *J. Microelectromech. Syst.* **2015**, *24* (6), 1663−1677.

(32) Kim, H.-S.; Melvin, D. K.; Patel, M.; Kim, J.; Cho, B.; Kim, D.-H. High-Performing MoS2-Embedded Si Photodetector. *Mater. Sci. Semicond. Process* **2017**, *71*, 35−41.

(33) Li, Y.; Xu, C.-Y.; Wang, J.-Y.; Zhen, L. Photodiode-like Behavior and Excellent Photoresponse of Vertical Si/Monolayer MoS2 Heterostructures. *Sci. Rep.* **2014**, *4* (1), 7186.

(34) Ismail, R. A.; Al-Samarai, A.-M. E.; Ali, A. Y. Preparation and Characteristics Study of CdS/Macroporous Silicon/C-Si Double Heterojunction Photodetector by Spray Pyrolysis Technique. *Optik* **2018**, *168*, 302−312.

(35) Roccaforte, F.; Filippo, F.; Raineri, V. Nanoscale Transport Properties at Silicon Carbide Interfaces. *J. Phys. D: appl. Phys.* **2010**, *43* (22), 223001.

(36) Kim, Y.; Kim, J.; Kim, H.; Jang, J. Quantum-Dots Photosensor with Wide Bandgap P-Type and N-Type Oxide Semiconductors for High Detectivity and Responsivity. *Adv. Mater. Technol.* **2020**, *5* (1), 1900857.

(37) Kremers, G.-J.; Hazelwood, K. L.; Murphy, C. S.; Davidson, M. W.; Piston, D. W. Photoconversion in Orange and Red Fluorescent Proteins. *Nat. Methods* **2009**, *6* (5), 355−358.

(38) Colinge, J.-P.; Colinge, C. A. *Physics of Semiconductor Devices*; Springer: Boston, Mass, 2006.

(39) Sze, S. M.; Yiming, L.; Ng, K. K. *Physics of semiconductor devices*; John wiley & sons, 2021.

(40) Dao, D. V. Study on silicon piezoresistive six-degree of freedom micro force-moment sensors and application to fluid mechanics. In *Doctoral thesis*; Ritsumeikan University, 2003.